Supplementary Material

Understanding monsoon controls on the energy and mass balance of glaciers in the Central and Eastern Himalaya

Authors: Stefan Fugger[1,2], Catriona L. Fyffe[3], Simone Fatichi[4], Evan Miles[1], Michael McCarthy[1,5], Thomas E. Shaw[1], Baohong Ding[6], Wei Yang[6], Patrick Wagnon[7], Walter Immerzeel[8], Qiao Liu[9], and Francesca Pellicciotti[1,3]

The Supplementary Material includes additional descriptions of data sets, extended figures, tables, methods and analysis, and is structured into these topics:

S1. Climatic and meteorological conditions

Average mean monthly 2 m air temperatures have a similar pattern at all study sites (Figure S1a), with a slow increase from January to a peak between July and August, just after peak monsoon, and a steeper decline from post-monsoon into winter. Incoming shortwave radiation (Figure S1b) shows a clear peak before monsoon onset at all sites. A smaller secondary peak is reached just after the monsoon in October at the Central Himalayan sites, but not at the Eastern Himalayan sites. Interruptions in monsoonal overcast conditions (break periods) seem to be more common at the eastern sites, leading to occasional secondary peaks in incoming shortwave radiation during monsoon. $LW_{\downarrow}$ follows a similar regime as Ta, with highest values reached during the core monsoon (Figure S1c). The yearly cycle of wind speeds (Figure S1d) varies considerably between sites. Common characteristics for most sites (except for Changri Nup) are that wind speeds are highest around December/January and that monsoonal wind speeds are generally higher than during the shoulder seasons. There is a clear difference in the seasonal evolution of precipitation between the Central (Lirung, Lantang, Yala, Changri Nup) and the Eastern Himalayan sites (24K, Parlung No.4, Hailuogou) (Figure S1e): relatively high mean monthly precipitation during the monsoon period is contrasted by comparably low precipitation outside of this period. The eastern sites have less pronounced monsoonal precipitation peaks, and more gradual changes in precipitation intensities over the annual cycle. The Parlung sites (24K and Parlung No.4) have two precipitation peaks: during spring and monsoon. Hailuogou exhibits the smoothest evolution over the annual cycle with a clear maximum in July. A simple monsoon index (MI) is calculated for each year including the study year as the ratio between monsoon precipitation and annual average precipitation (Figure S1e). This value tends to be higher in the Central Himalaya compared to the sites on the South-Eastern Tibetan Plateau.

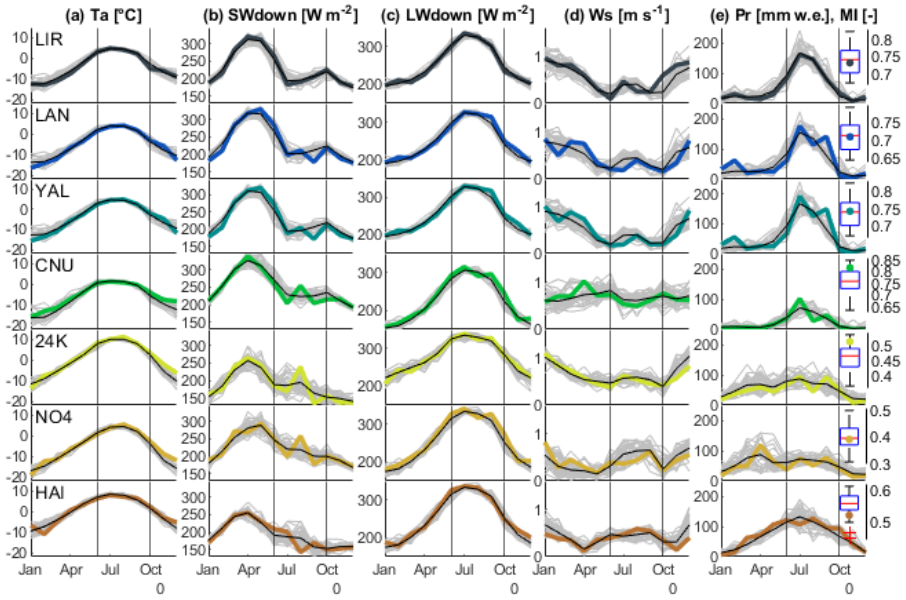

Figure S1. Monthly climatology derived from ERA5-Land for 1981-2019 (grey background lines), along with the monthly averages (black lines) and the study year at each glacier (colored lines). Plotted meteorological variables are **(a)** mean air temperature (Ta), **(b)** incoming shortwave radiation ($SW_{\downarrow}$), **(c)** incoming longwave radiation ($LW_{\downarrow}$), **(d)** wind speed (Ws) and **(e)** monthly precipitation sums (Pr). Black vertical lines indicate the average region-wide monsoon season. Boxplots show the monsoon index (MI) over ERA5-Land period as the fraction of monsoonal (June-September) to annual precipitation, with the colored dot indicating the value for the study year.

S2. Data selection and monsoon definition

The records and periods were chosen under considering the following criteria:

- Data availability
- Completeness of records (few or no data gaps)
- Availability of complete forcing data for modelling, including precipitation records
- Availability of ablation stake measurements or other recordings of surface lowering (e.g. Ultrasonic Depth Gauge)
- Highest quality and reliability of records (No unrealistic/erroneous/disagreeing records)
- Possibility to substitute from other stations when criteria 1.-4. were not met

At each site, we define the onset and recession date of monsoon based on visual inspection of the AWS records (Figures SS2 to SS8) following this procedure:

1. Inspect $SW\downarrow$ to identify a period with sustained cloud overcast and with few interruptions therein, lowering $SW\downarrow$
2. Inspect $LW\downarrow$ and compare the timing of constantly higher $LW\downarrow$ with the above
3. Identify the period of increased rainfall frequency and intensity
4. Inspect the relative humidity to see whether the timing of sustained humid conditions would agree with the above
5. Identify a plateau in average air temperature and dampening of the daily air temperature amplitude
6. Inspect wind speed to identify a regime change (mean and amplitude)

This was the general procedure followed, but the order was varied, when one or the other variable provided a clearer indication. We note, that in some cases, where heavy cloud cover and rainy conditions dominate the local weather from spring to autumn (e.g. Hailuogou, 24K) this distinction was less clear than in others, and some uncertainty remains around the exact monsoon onset and cessation dates at those study sites.

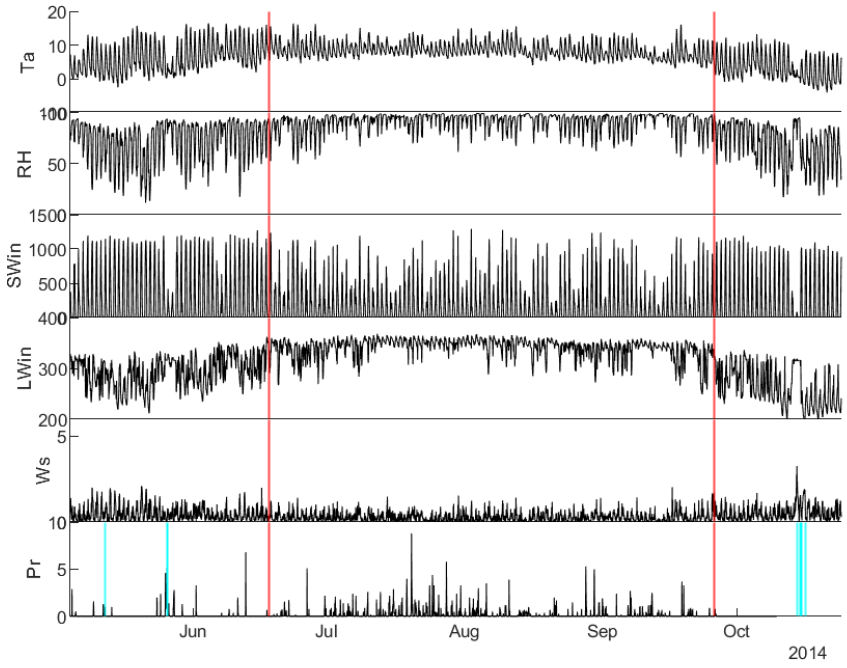

Figure S2. Meteoroligical observations on Lirung during the ablation season recorded by AWS; Red vertical lines indicate monsoon onset and end; cyan indicates time steps with snow cover at the AWS location, as determined from α (>0.5)

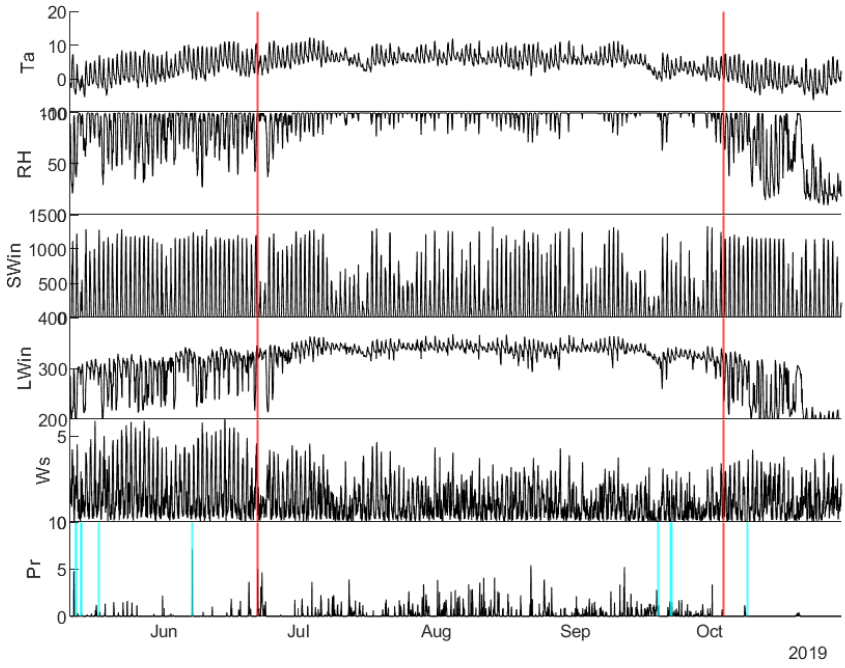

Figure S3. Meteoroligical observations on Langtang during the ablation season recorded by AWS; Red vertical lines indicate monsoon onset and end; cyan indicates time steps with snow cover at the AWS location, as determined from α (>0.5)

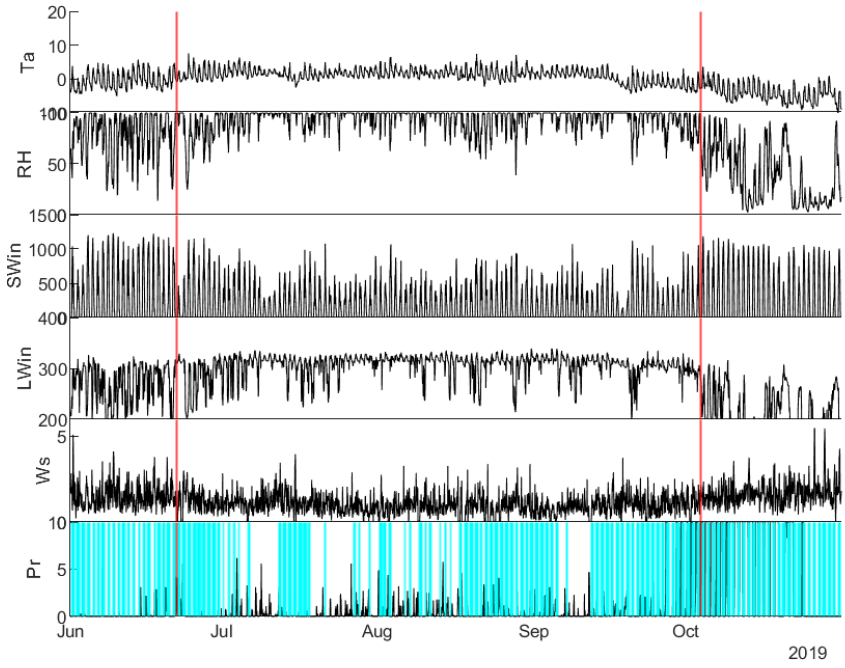

Figure S4. Meteoroligical observations on Yala during the ablation season recorded by AWS; Red vertical lines indicate monsoon onset and end; cyan indicates time steps with snow cover at the AWS location, as determined from α (>0.5)

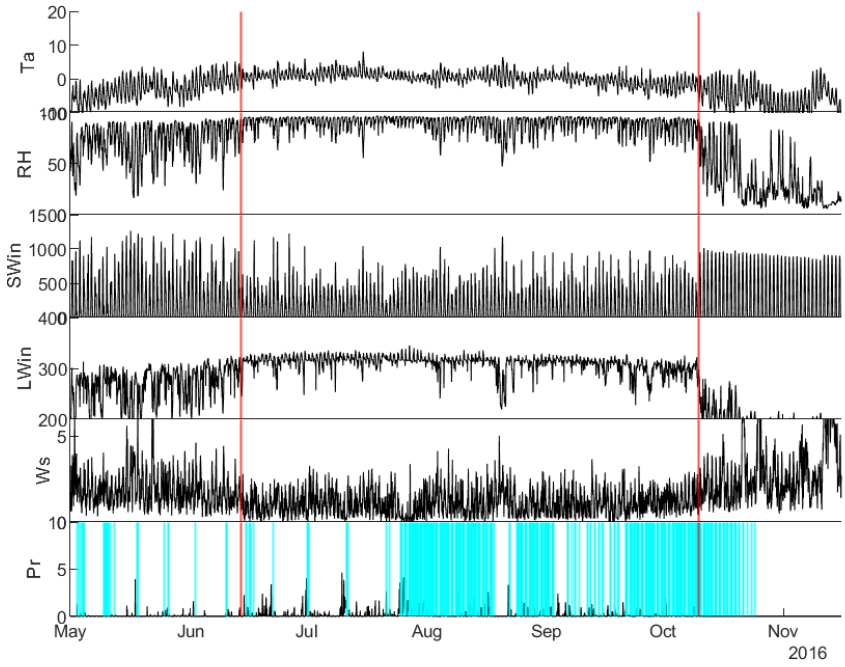

Figure S5. Meteoroligical observations on Changri Nup during the ablation season recorded by AWS; Red vertical lines indicate monsoon onset and end; cyan indicates time steps with snow cover at the AWS location, as determined from α (>0.5)

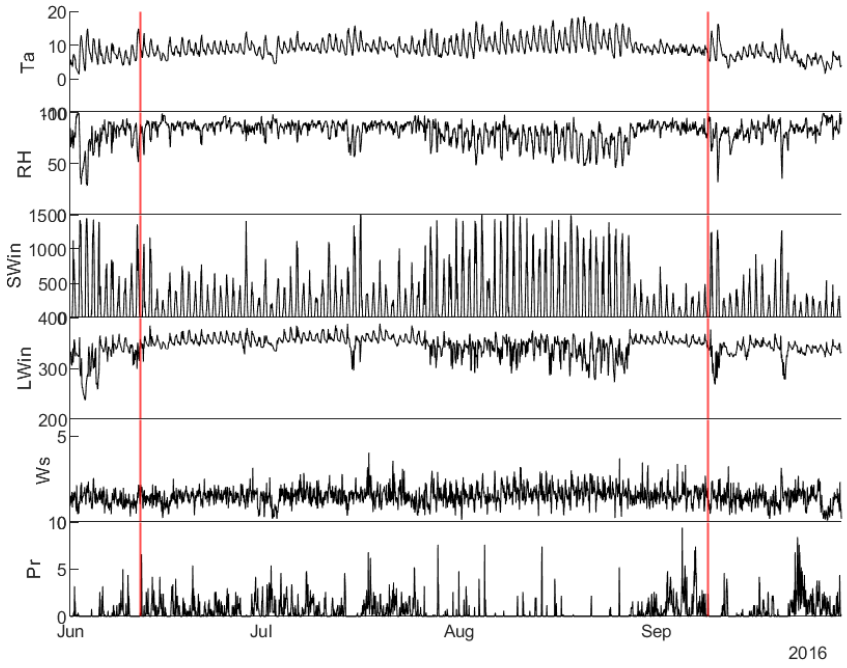

Figure S6. Meteoroligical observations on 24K during the ablation season recorded by AWS; Red vertical lines indicate monsoon onset and end; cyan indicates time steps with snow cover at the AWS location, as determined from α (>0.5)

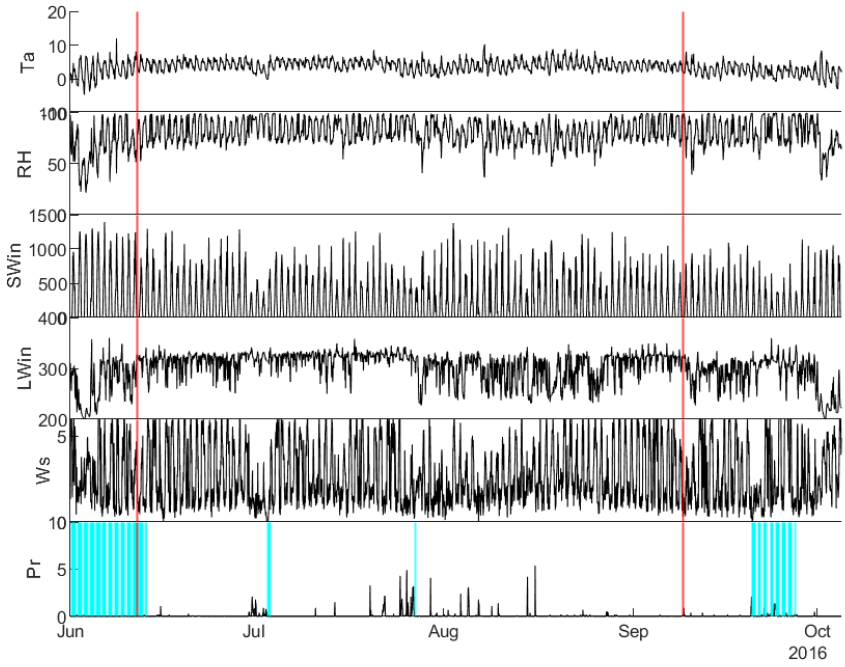

Figure S7. Meteoroligical observations on Parlung No.4 during the ablation season recorded by AWS; Red vertical lines indicate monsoon onset and end; cyan indicates time steps with snow cover at the AWS location, as determined from α (>0.5)

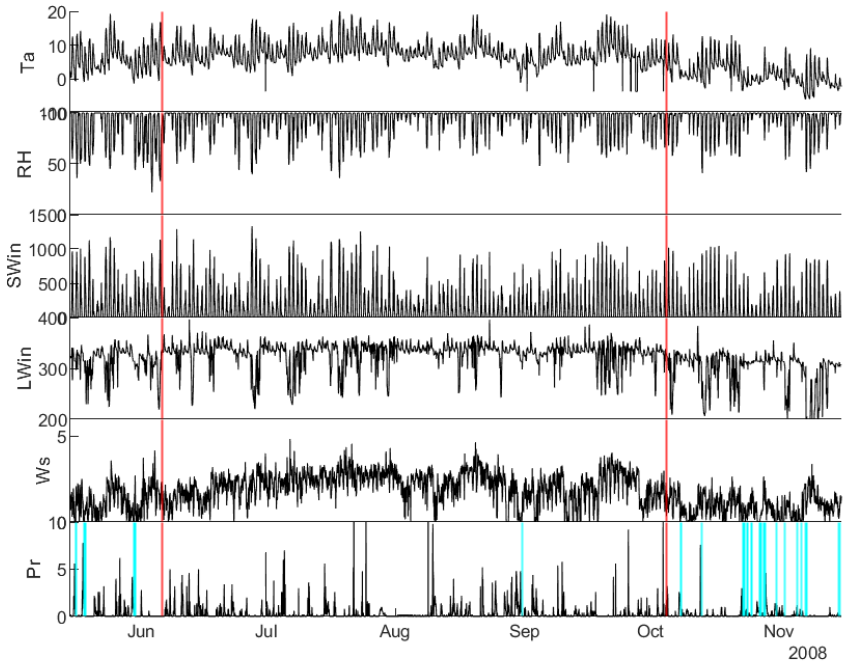

Figure S8. Meteoroligical observations on Hailuogou during the ablation season recorded by AWS; Red vertical lines indicate monsoon onset and end; cyan indicates time steps with snow cover at the AWS location, as determined from α (>0.5)

Table S1. Air temperature Ta, mean daily precipitation Pr_d, relative humidity RH, vapor pressure deficit vpd, mean cloud-cover fraction ccf, temperature gradient between surface and air δ_T, wind speed Ws and the percentage of time during which the debris is modelled to hold intercepted water In for each site and season, also indicating percent changes between the sub-seasons.

		$Ta\,[°C]$			$Pr\,[mm\,d^{-1}]$			$Ws\,[m\,s^{-1}]$			$RH\,[-]$			$vpd\,[Pa]$			$\delta_T\,[°C\,m^{-1}]$			$In\,[\%]$		
		pre	*mon*	*post*	*pre*	*mon*	*post*	*pre*	*mon*	*post*	*pre*	*mon*	*post*	*pre*	*mon*	*post*	*pre*	*mon*	*post*	*pre*	*mon*	*post*
LIR	mean	6.4	8.5	3.3	1.8	4.4	0.1	0.47	0.27	0.52	68.1	90.8	67.1	318.8	103.5	262.5	1.19	0.78	0.89	40.1	74.0	26.4
	Δ		*2.1*	*-5.2*		*2.6*	*-4.3*		*-0.19*	*0.24*		*22.6*	*-23.6*		*-215.3*	*159.1*		-0.40	0.10		33.9	-47.6
LAN	mean	3.1	5.7	0.5	2.2	5.9	0.3	1.79	1.10	1.27	80.7	96.9	56.3	152.1	28.7	282.3	1.02	0.97	0.95	38.8	75.3	9.5
	Δ		*2.6*	*-5.2*		*3.7*	*-5.6*		*-0.68*	*0.17*		*16.2*	*-40.6*		*-123.5*	*253.6*		-0.05	-0.02		36.5	-65.8
YAL	mean	-2.6	1.2	-4.1	2.0	17.0	345.2	1.74	1.00	1.68	69.8	93.0	39.4	156.1	47.1	278.4	-0.36	-0.96	-0.89	-	-	-
	Δ		*3.8*	*-5.3*		*15.1*	*328.2*		*-0.74*	*0.67*		*23.2*	*-53.6*		*-109.1*	*231.4*		-0.59	0.07		-	-
CNU	mean	-2.8	0.4	-4.7	0.5	3.1	0.0	1.88	1.09	2.48	71.2	89.2	39.3	147.4	68.1	270.5	1.69	0.25	0.89	16.2	79.3	5.3
	Δ		*3.1*	*-5.1*		*2.6*	*-3.1*		*-0.79*	*1.39*		*18.1*	*-50.0*		*-79.3*	*202.3*		-1.44	0.64		63.1	-74.0
24K	mean	7.3	9.8	6.9	6.5	13.8	18.3	1.33	1.56	1.35	73.1	80.6	81.2	279.3	238.0	189.2	1.86	0.73	0.18	56.8	79.1	84.3
	Δ		*2.5*	*-2.9*		*7.3*	*4.5*		*0.22*	*-0.21*		*7.4*	*0.7*		*-41.3*	*-48.8*		-1.13	-0.55		22.3	5.2
NO4	mean	0.9	4.1	0.4	2.4	1.7	0.7	2.96	2.67	3.23	65.7	81.3	73.1	230.8	153.9	173.9	-0.78	-2.01	-0.62	-	-	-
	Δ		*3.2*	*-3.7*		*-0.7*	*-1.0*		*-0.28*	*0.56*		*15.7*	*-8.3*		*-76.9*	*20.0*		-1.22	1.39		-	-
HAI	mean	6.1	7.8	-2.1	8.5	7.8	2.4	1.23	2.15	0.93	81.3	92.3	90.6	182.4	83.8	52.3	-2.08	-2.61	0.38	99.8	100.0	75.6
	Δ		*1.7*	*-9.9*		*-0.7*	*-5.4*		*0.91*	*-1.22*		*10.9*	*-1.6*		*-98.6*	*-31.5*		-0.53	2.99		0.2	-24.4

S3. Aerodynamic resistance and aerodynamic roughness

The aerodynamic resistance quantifies the ability of the surface boundary layer to resist or intensify turbulent transport of momentum, heat and water vapor. We calculate the aerodynamic resistances to heat flux r_{ah} and water vapor r_{aw} using the simplified solution of the Monin-Obukhov similarity theory, introduced by Mascart et al. (1995) and implemented into the ISBA landsurface model Noilhan and Mahfouf (1996). This parameterization of the full Monin-Obukhov similarity theory (Monin and Obukhov, 1954) is computationally less demanding, while providing concurring results (Fatichi, 2010). In T&C, the common assumption is of a single aerodynamic resistance (e.g. Viterbo and Beljaars, 1995; Ivanov et al., 2008), is used, such that $r_{ah} = r_{aw}$. To gain r_{ah}, in the simplified solution, a bulk transfer coefficient C_h can be expressed as:

$$C_h = 1\frac{r_{ah}}{W_s} = C_n F_h(R_{i_B}) \tag{17}$$

where the neutral transport coefficient C_n is:

$$C_n = \frac{k^2}{ln[(z_{atm} - d)/z_{om}]^2} \tag{18}$$

and the empirical function of the bulk Richardson number R_{ib} is:

$$F_h(Ri_B) = \begin{cases} \left[1 - \frac{15Ri_B}{1+c_h\sqrt{|Ri_B|}}\right]\left[\frac{ln[(z_{atm}-d)/z_{om}]}{ln[(z_{atm}-d)/z_{oh}]}\right], & \text{if } Ri_B \leq 0 \\ \left[\frac{1}{1+15Ri_B\sqrt{1+5Ri_B}}\right]\left[\frac{ln[(z_{atm}-d)/z_{om}]}{ln[(z_{atm}-d)/z_{oh}]}\right], & \text{if } Ri_B > 0 \end{cases} \tag{19}$$

wherein

$$c_h = 15c_h^* C_n[(z_{atm} - d]^{p_h}\left[\frac{\ln[(z_{atm} - d)/z_{om}]}{\ln[(z_{atm} - d)/z_{oh}]}\right] \tag{20}$$

$$c_h^* = 3.2165 + 4.3431\mu + 0.5360\mu^2 - 0.0781\mu^3 \tag{21}$$

$$p_h = 0.5892 - 0.1571\mu + 0.0327\mu^2 - 0.0026\mu^3 \tag{22}$$

$$\mu = \ln(z_{om}/z_{oh}) \tag{23}$$

To prevent a full inhibition of turbulent transport under wind-still conditions (r_{ah} would become infinite), when $Ws < 0.05\,m\,s^{-1}$, we calculate C_h following Beljaars (1995):

$$C_h = \frac{1}{r_{ah}} = 0.15\Big[\frac{g\nu}{0.5(T_s + T_a)Pr^2}\Big]^{1/3}(T_s - T_a)^{1/3} \tag{24}$$

where $\nu = 1.5110^{-5}[m^2 s^{-1}]$ and the Prandtl number $Pr = 0.71$.

As a consequence of the assumption explained above (r_{ah} = r_{aw}), also the aerodynamic roughnesses of heat and water vapour are used as equal (z_{ow} = z_{oh}) and $z_{0h} = z_{0w} = 0.1 z_{0m}$. For the ratio r between the roughness lengths of water vapour, heat and momentum, $r = 0.1$ is a value based on (Brutsaert, 1982), often implemented in land surface models (e.g. Noilhan and Mahfouf, 1996), and is also used in TC. This ratio remains poorly constrained, not least due to the difficulties in measuring or deriving surface roughnesses (Miles et al., 2017; Quincey et al., 2017). Three values have been suggested in the literature: $r = 1$ (e.g. Reid and Brock, 2010), $r = 0.1$ (e.g. Giese et al., 2020) $r = 0.05$ (Steiner et al. 2018), who derived this value for Lirung from flux tower experiments. Since here, z_{0h}, z_{0w} and z_{0m} were effectively optimised together at the debris-covered glaciers, the turbulent fluxes remain insensitive to the choice of this ratio.

S4. Extended Results

Table S2. RMSE values for modelled vs. measured T_s at all sites. Measured T_s were derived from $LW_{\downarrow}$ and $LW_{\uparrow}$ measurements considering the entire modelling period at all sites

		Lirung	Langtang	Yala	Changri Nup	24K	Parlung No.4	Hailuogou
RMSE	[°C]	2.3	2.2	2.99	2.6	1.8	2.89	1.0

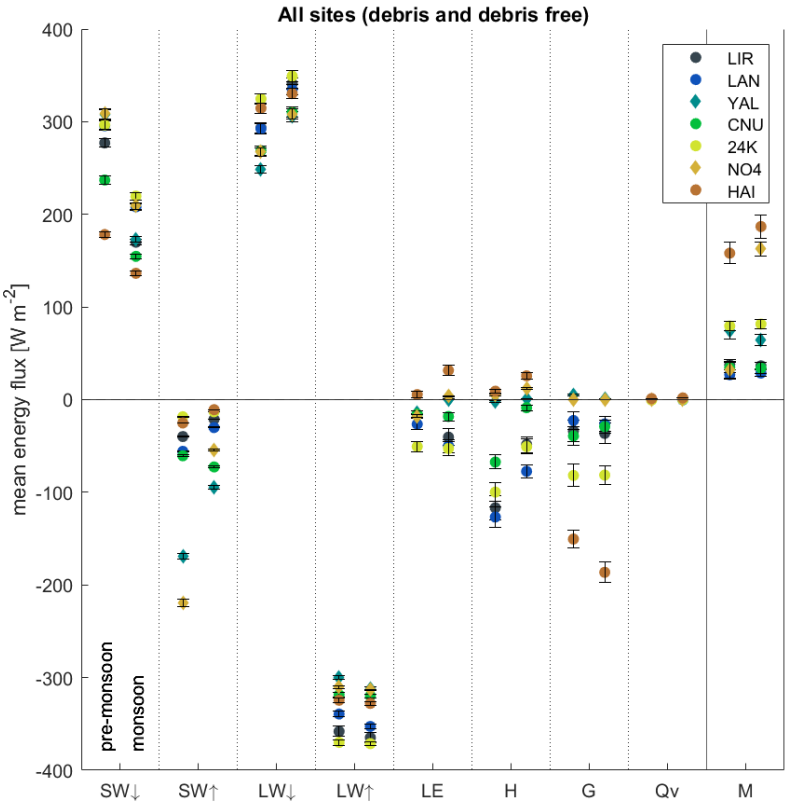

Figure S9. All energy balance components of all glaciers in comparison, split into pre-monsoon and monsoon; black bars indicate the uncertainty range;

Table S3. Mean energy balance components at each site and for pre-monsoon (pre), monsoon (mon), and post-monsoon (post) periods, as well as flux magnitude changes from pre-monsoon to monsoon, and monsoon to post-monsoon. All values are in $W\,m^{-2}$.

fluxes in W/m2		$SW_{\downarrow}$			$SW_{\uparrow}$			$LW_{\downarrow}$			$LW_{\uparrow}$			LE		
		pre	*mon*	*post*	*pre*	*mon*	*post*	*pre*	*mon*	*post*	*pre*	*mon*	*post*	*pre*	*mon*	*post*
LIR	mean	277.1	170.0	224.1	-39.8	-21.1	-41.3	293.3	341.2	264.0	-358.1	-364.8	-340.4	-16.0	-40.4	-1.9
	Δ		*-107.1*	*54.1*		*18.7*	*-20.2*		*47.9*	*-77.2*		*-6.7*	*24.4*		*-24.4*	*38.5*
LAN	mean	295.6	208.1	262.4	-55.9	-30.1	-48.6	292.3	334.7	238.6	-339.3	-352.8	-326.1	-26.4	-49.9	-5.8
	Δ		*-87.5*	*54.3*		*25.7*	*-18.4*		*42.3*	*-96.0*		*-13.5*	*26.7*		*-23.5*	*44.1*
YAL	mean	307.7	172.7	271.8	-169.4	-94.4	-195.0	248.5	305.5	212.3	-299.8	-311.6	-287.1	-13.7	0.1	-12.2
	Δ		*-135.0*	*99.1*		*75.0*	*-100.6*		*57.0*	*-93.2*		*-11.7*	*24.4*		*13.7*	*-12.3*
CNU	mean	237.1	154.7	258.1	-60.6	-72.7	-126.0	268.8	310.2	196.4	-318.7	-319.7	-300.4	-15.7	-18.1	-3.1
	Δ		*-82.4*	*103.4*		*-12.1*	*-53.3*		*41.5*	*-113.8*		*-1.0*	*19.3*		*-2.5*	*15.0*
24K	mean	296.6	219.7	140.9	-18.5	-13.0	-8.3	324.6	349.3	336.6	-369.9	-371.3	-351.0	-50.6	-52.7	-40.0
	Δ		*-76.9*	*-78.8*		*5.4*	*4.7*		*24.7*	*-12.7*		*-1.3*	*20.3*		*-2.1*	*12.7*
NO4	mean	308.5	209.1	197.3	-219.6	-54.8	-81.5	267.5	308.2	261.5	-310.3	-313.4	-310.5	-17.6	3.6	-18.5
	Δ		*-99.5*	*-11.8*		*164.8*	*-26.7*		*40.7*	*-46.7*		*-3.1*	*2.9*		*21.2*	*-22.1*
HAI	mean	178.2	136.4	105.8	-25.2	-10.8	-28.4	314.6	330.3	273.1	-324.5	-327.9	-309.1	5.4	31.6	-4.8
	Δ		*-41.8*	*-30.6*		*14.4*	*-17.6*		*15.7*	*-57.2*		*-3.4*	*18.8*		*26.2*	*-36.4*

fluxes in W/m2		H			G			dG			Qv			M		
		pre	*mon*	*post*	*pre*	*mon*	*post*	*pre*	*mon*	*post*	*pre*	*mon*	*post*	*pre*	*mon*	*post*
LIR	mean	-116.7	-48.4	-86.5	-33.7	-36.4	-18.7	5.6	0.0	16.6	0.0	0.0	0.0	-37.5	-36.5	-19.0
	Δ		*68.3*	*-38.0*		*-2.7*	*17.8*		*-5.6*	*16.6*		*0.0*	*0.0*		*1.0*	*-17.5*
LAN	mean	-126.7	-77.4	-111.4	-22.5	-26.2	-7.8	2.2	0.0	27.3	0.0	-0.3	0.0	-26.9	-28.7	-10.4
	Δ		*49.3*	*-34.1*		*-3.7*	*18.4*		*-2.2*	*27.3*		*-0.3*	*0.3*		*-1.8*	*-18.4*
YAL	mean	-2.3	0.5	1.4	4.7	0.9	0.0	4.7	0.9	0.0	0.0	-0.2	-4.1	-74.8	-64.6	-0.3
	Δ		*2.8*	*0.9*		*-3.8*	*-0.9*		*-3.8*	*-0.9*		*-0.2*	*-3.9*		*10.2*	*-64.3*
CNU	mean	-67.4	-8.7	-36.1	-39.2	-29.1	10.4	17.1	1.8	10.6	0.0	0.0	0.0	-34.6	-34.1	-0.2
	Δ		*58.7*	*-27.4*		*10.1*	*39.5*		*-15.3*	*8.9*		*0.0*	*0.0*		*0.5*	*-33.9*
24K	mean	-99.8	-50.8	-24.4	-81.8	-81.4	-53.1	0.3	0.0	0.0	-0.3	0.2	0.6	-79.5	-81.6	-53.7
	Δ		*49.0*	*26.4*		*0.4*	*28.4*		*-0.3*	*0.0*		*0.6*	*0.4*		*-2.1*	*-27.9*
NO4	mean	4.7	12.3	5.8	0.2	0.1	0.1	0.2	0.1	0.0	0.2	0.2	0.0	-32.3	-162.6	-54.1
	Δ		*7.6*	*-6.6*		*-0.1*	*-0.1*		*-0.1*	*-0.1*		*0.0*	*-0.2*		*-130.4*	*-108.5*
HAI	*mean*	9.1	25.7	-9.9	-150.4	-186.4	-16.5	1.8	0.5	17.6	1.2	1.9	0.1	-158.1	-186.8	-36.9
	Δ		*16.6*	*-35.5*		*-35.9*	*169.9*		*-1.4*	*17.2*		*0.7*	*-1.8*		*-28.7*	*-149.9*

S5. Sensitivity of seasonal flux changes to elevation and debris thickness

Assuming that the strongest changes in meteorological forcing with elevation would be the Ta, which in turns controls the precipitation partition and the albedo, we re-run the model varying Ta under applying a temperature lapse rate of $0.6\,°C/100m$ and, for the debris-covered sites, by varying also the debris thickness in the range 10-80 cm (for ranges and steps see Table S4). Using the station-measured, accumulated albedo is not appropriate during this experiment, due to changing snow conditions with varying elevation. We therefore include the parameterisation introduced by Ding et al. (2017) for modelling α. From the resulting range of EB flux outputs, we calculate the range of expected changes for the entire ablation zone when moving from pre-monsoon to monsoon (Δ-range). This allows us to place our results in the context of the changes that can be expected over the entire ablation zone, given its elevation span and debris thickness variability. Figure 8 shows that even accounting for the range of conditions across each glacier ablation area, the pattern of pre-monsoon to monsoon difference in flux components, and importantly M, remain similar for debris-covered sites: The Δ-range of M stays within the uncertainty range, with the exception of Langtang, where the unrealistic combination of relatively thin debris and low elevation causes high M Δ-range. This lends confidence to the results obtained at the individual AWS locations. Although we adjusted forcing data for elevation in this exercise, we could not represent the effects of variable debris thicknesses in modifying $2\,m$ meteorological variables (Steiner and Pellicciotti, 2016; Shaw et al., 2016). This comes with the assumption that surface-atmosphere interactions are negligible compared to the altitudinal patterns and temporal changes. While this might be acceptable at thicker debris sites, it is more questionable at Hailuogou, where the observations were taken above thin and cold debris. However, also at this site, the Δ-range ends up to be small ($5\ W\,m^{-2}$) and close to zero when debris between 10 and $80\,cm$ thickness is applied artificially.

Table S4. Ranges of elevations and debris thicknesses used for the sensitivity runs, including the glacier terminus elevation (min), the AWS elevation (AWS) and the upper debris limit on debris-covered glaciers or to the approximated ELA elevation on clean-ice glaciers (max). We also show the range of debris thicknesses h_m modelled for debris-covered glacier sites. All combinations of elevations and debris thicknesses were used.

Glacier		**Lirung**	**Langtang**	**Yala**	**Changri Nup**	**24K**	**Parlung No.4**	**Hailuogou**
min	$[m.asl]$	3990	4500	5170	5270	3910	4620	2980
AWS	$[m.asl]$	4076	4557	5350	5471	3900	4800	3550
max	$[m.asl]$	4400	5600	5400	5600	4200	5400	3700
h_d $[cm]$	10, 20, 30, 40, 50, 60, 70, 80							

S6. Controls on turbulent fluxes

To understand which climatic variables of the boundary layer control the turbulent fluxes on debris-covered glaciers, regression models were fitted to the modelled values of the energy fluxes H and LE at the hourly timescale, and for pre-monsoon and monsoon separately. A summary figure is given in the main text (Figure 4.5). Values of $0\,W\,m^2$ were removed from LE, which appear at timesteps when no water is available at the debris surface. The predictive power of three variables and their combination was determined and evaluated with adjusted R^2: (i) The temperature gradient between surface and air $\delta_T\,[°C^{-1}]$:

$$\delta_T(t) = Ts(t) - Ta(t) \tag{25}$$

(ii) the vapour pressure deficit $vpd\,[Pa]$:

$$vpd(t) = esat(t) - ea(t) \tag{26}$$

where $ea\,[Pa]$ is the vapor pressure and $esat\,[Pa]$ is the saturated vapor pressure, and (iii) the wind speed Ws. Univariate quadratic regression models fitted for single predictors had the form:

$$y(t) = a + bx(t) + cx(t)^2 \tag{27}$$

and multivariate linear regression models fitted for multiple predictors had the form:

$$y(t) = a + bx_1(t) + bx_2(t) + bx_3(t) \tag{28}$$

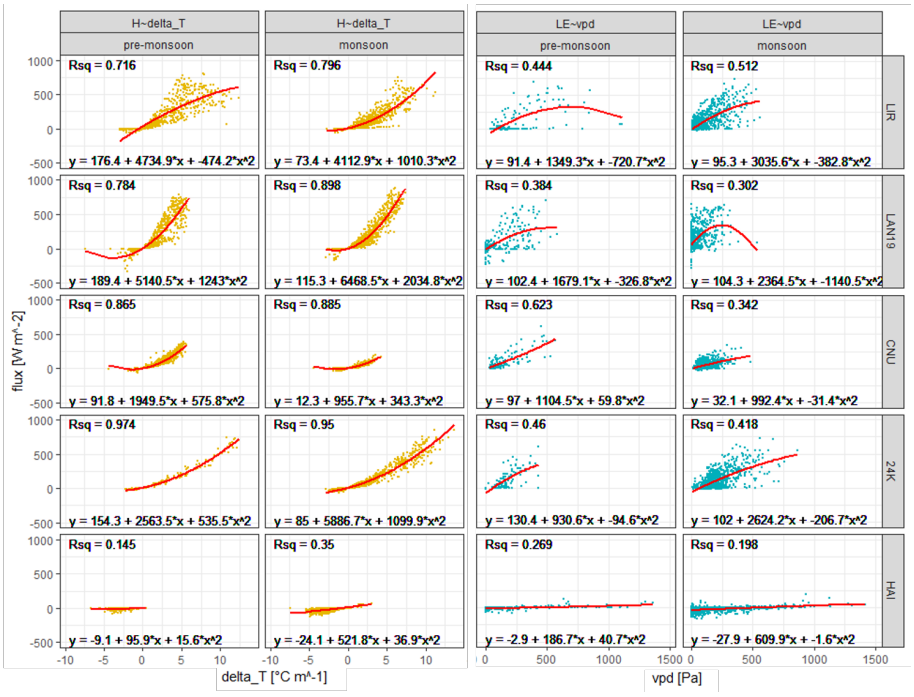

Figure S10. (a) Regression plots for temperature gradient between surface and air δ_T against H and vapor pressure deficit vpd against LE for the debris cover sites, seperately for pre-monsoon and monsoon. Fitted model (red line), adj.R^2 and model equation.

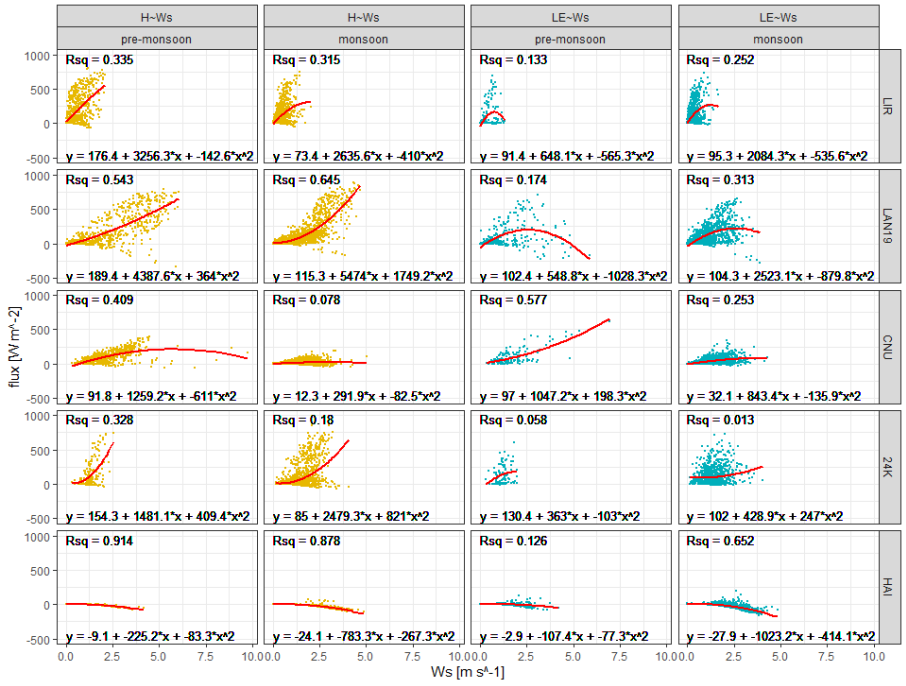

Figure S11. (a) Regression plots for wind speed Ws against H and LE for the debris cover sites, seperately for pre-monsoon and monsoon. Fitted model (red line), adj.R^2 and model equation.